nature geoscience | SUPPLEMENTARY INFORMATION
DOI: 10.1038/NGEO1521

Possible links between long-term geomagnetic variations and whole-mantle convection processes

Biggin, A.J., Steinberger, B., Aubert, J., Suttie, N., Holme, R., Torsvik, T.H., van der Meer, D.G., van Hinsbergen, D.J.J.

Description of numerical model of mantle flow

The numerical model closely follows Steinberger and Torsvik[75] (henceforth referred to as ST12) where it has been described in detail. In brief, mantle flow is computed with a method based on spherical harmonics, considering radial viscosity variations. Input of subducted slabs (cold thermal density anomalies) in the upper mantle is prescribed based on 300 Myr subduction history. Radial heat flow from the core to the mantle is computed with a CMB thermal density anomaly (compared to an adiabatic profile) of 1.2 % (1126 K for expansivity $1.065418 .10^{-5}$ /K), diffusivity 0.95 * 10-6 m^2/s, heat capacity 1250 J/kg/K and density 5556 kg/m^3. The model also contains a basal layer (chemically 2.3 % heavier; initially 70 km thick everywhere). Thermal and chemical density anomalies are advected with the flow.

After 140 Ma, we consider subduction locations, convergence rates and age of subducted lithosphere in computing slab input. Before 175 Ma, only subduction locations are considered, assuming constant convergence rate and age, as they are unknown. A linear interpolation is used to smoothen the transition between 140 and 175 Ma - see ST12 for details. Consequently, the increase in subduction input prior to 140 Ma (figure 2a) may be a model artifact, but the decrease after ~90 Ma is probably real.

All CMB heat flow patterns were analysed in the palaeomagnetic reference frame (i.e. after applying rotations due to observed TPW) which is the appropriate one for interpreting them as boundary conditions for the geodynamo. In only one analysis (figure 4 in the main text), was the TPW implied by the model itself (rather than independent measurements) used for the correction.

The model cases shown and discussed here are all similar to the case shown in Figure 5 of ST12, with the only differences as follows:

Case 1 (black line in top panel, and bottom left panel in figure 2) uses a stronger depth dependence of thermal expansivity α. Whereas in ST12 absolute density anomalies are advected (corresponding to assuming α is inversely proportional to radially varying reference density), we assume here a radial

DOI: 10.1038/NGEO1521

profile of α corresponding to the lower mantle profile of Steinberger and Calderwood (2006) but extrapolated to the surface. Consequently, in this model density anomalies corresponding to subducted slabs become considerably smaller as the anomalies sink to the lower mantle (as seen from the blob indicated by an asterisk in the figure 2b). It is computed for incompressible flow.

Case 2 differs from ST12 only in that it is initiated at 400 Ma instead of 300 Ma, without subduction input between 400 and 300 Ma, such that a basal thermal boundary layer has developed, and heat flow has decreased to realistic values by 300 Ma. Case 2A is initiated at 300 Ma with the model output of Case 2 at 0 Ma. Case 2B continues this run using the output of Case 2A at 0Ma for its staring condition at 300 Ma. These indicate how CMB heat flow might be different due to the fact that subduction was going on prior to 300 Ma. For longer model runs it appears to tend towards lower values, more consistent with independent estimates[66].

Case 3 is again initiated at 400 Ma, and with the stronger depth dependence of α as in Case 1. After 200 Ma, results differ from Case 1 mainly because compressibility is considered, somewhat reducing flow speeds in the lower mantle caused by subducted slabs. Case 3A again consists of a rerun using as initial conditions at 300 Ma, the output of Case 3 at 0 Ma.

In figure 2a, the strong initial increase in cases 2 and 3 after ~250 Ma, approximately doubling heat flow is due to subduction initiation, which is global in our model. Similarly the strong decrease in Case 1 after 0 Ma, reducing heat flow by more than a factor 3, is due to global subduction cessation in the model. These model features are meant to illustrate the effect of subduction initiation and cessation, which are in reality probably more regional in nature through most or all of Earth history. Hence such heat flow variations are likely to occur regionally, but for global heat flow variations, the variability in Case 2 after ~150 Ma, and in Case 2A (i.e. in the order of 20%) is probably more representative.

Supplementary Figure 1 contains additional results for the following model cases:

Case 4: As case 3, but initiated without subduction between 1010 Ma and 300 Ma. In this case, plumes rising from the CMB to the surface have fully developed in the model prior to the insertion of slabs at 300 Ma. Because of the strong decrease of thermal expansivity, slabs have in this case globally a rather small effect on CMB heat flow.

Case 5: As case 2, but initiated without subduction between 1050 and 300 Ma, such that again plumes have developed prior to 300 Ma. In this case, the effect of slabs on CMB heat flow is stronger than in Case 4, but weaker than in Case 2.

Case 6: As case 2, but with mantle internal heating increased by a factor 10/3, i.e. from about 6 TW to about 20 TW. This strong increase in internal heating only leads to a minor decrease in CMB heat flow, and primarily leads to the mantle heating up in the model.

Case 7: As case 3, but internal heating incrased by factor 10/3. Again, effect on CMB heat flow is minor.

Equatorial CMB heat flow and hemispherical asymmetry

Supplementary figure 1a shows that the model in all cases displays no correlation between global CMB heat flow and reversal frequency over any significant time period. The output heat flow at equatorial latitudes is better correlated with geomagnetic reversal frequency in some of our cases (supplementary figure 1b,c) than is the global heat flow. In cases 2, 2A, 5, and 6, there is some similarity in the shapes of the equatorial output curves with that of the reversal frequency although the transitions in the CMB heat flow occur a little later than would be required. In those cases incorporating stronger decreases of thermal expansivity with depth (cases 1, 3, 4, and 7), the correspondence disappears entirely.

A more robust observation is that in almost all cases, there was enhanced hemispherical symmetry (about both the equator and any meridian) of CMB heat flow corresponding to the time of the CNS (supplementary figure 1d,e). This could be significant in light of observations of dynamo simulations tending to produce more reversals under conditions of hemispherically asymmetric forcing[14,64]. Enhanced symmetry of CMB heat flow conditions may have played a role (potentially alongside a minimum in the equatorial heat flow) in causing the CNS to occur when it did. In practically all cases, CMB heat flow increased progressively higher in the northern hemisphere relative to the southern hemisphere during the last 100 Myr resulting in enhanced equatorial asymmetry (supplementary figure 1d, figure 2). This also provides a potential explanation for the rise in reversal frequency through the Cainozoic when total subduction flux fell (supplementary figure 1a) and true polar wander was minimal.

Implications of observed TPW rotations for modelled equatorial CMB heat flow

In general, differences in the equatorial CMB heat flow produced by interpreting the model outputs in the mantle versus the palaeomagnetic reference frames were small because, during the time period at which these differed (> 100 Myr), the heat flow heterogeneities were still in the process of being established.

We considered it instructive to perform an analysis, analogous to that reported in figure 5 of the main text, using the CMB heat flow pattern produced by a model (Case 2) for the present day (shown in figure 3c of the main text) in place of the SMEAN tomographic model. The aims of this analysis were: (1) to gain insight into how much variation in equatorial heat flow could be produced by actual observed TPW rotations (of much smaller magnitude than those produced by the model and used in the analysis shown in figure 5 of the main text) and (2) to provide a test of how well the model captured the fine-scale features of the present-day mantle as inferred from seismology.

Supplementary figure 2 shows the results. Even these much smaller rotations produce changes in the average equatorial heat flow of a magnitude equal to several tens of percent of the unrotated value. This

DOI: 10.1038/NGEO1521

indicates that the degree of heterogeneity predicted by the model is sufficient to allow substantial variations in the equatorial heat flow to result from realistic TPW rotations. The actual time series of heat flow variations shows some anticorrelation with that inferred from the SMEAN model subject to the same rotations (figure 5). This suggests that, although this model does a reasonable job at producing thermochemical piles similar in shape and location to observed LLSVPs, it does not capture well the finer scale, high heat flow (fast shear wave) features of the real Earth's mantle.

Supplementary Reference

Steinberger, B. and A. Calderwood (2006). Models of large-scale viscous flow in the Earth's mantle with constraints from mineral physics and surface observations, Geophys. J. Int., 167, 1461-1481.

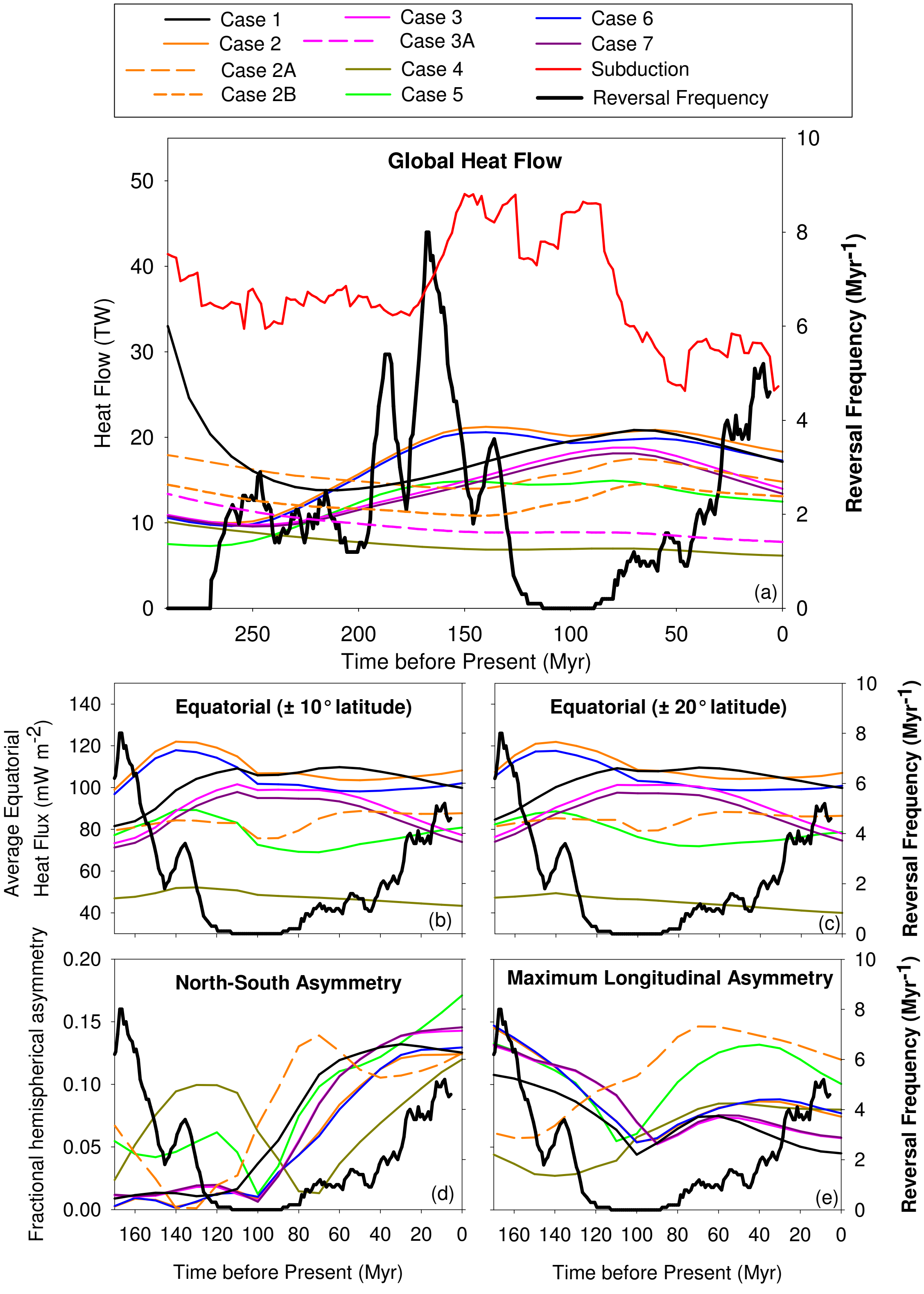

Supplementary Figure 1: (a) Mantle flow model outputs of total CMB heat flowin comparison to geomagnetic reversal frequency (b,c) the same for average equatorial heat flux. (d,e): measures of hemispherical asymmetry calculated as the difference between the net heat flow in the two hemispheres normalised by their average. In (e) the dividing line of longitude was selected at each time step to maximise the asymmetry. The period of comparison is restricted to 0-170 Ma to minimise effects relating to the onset of subduction at 300 Ma. See text for details of models.

DOI: 10.1038/NGEO1521

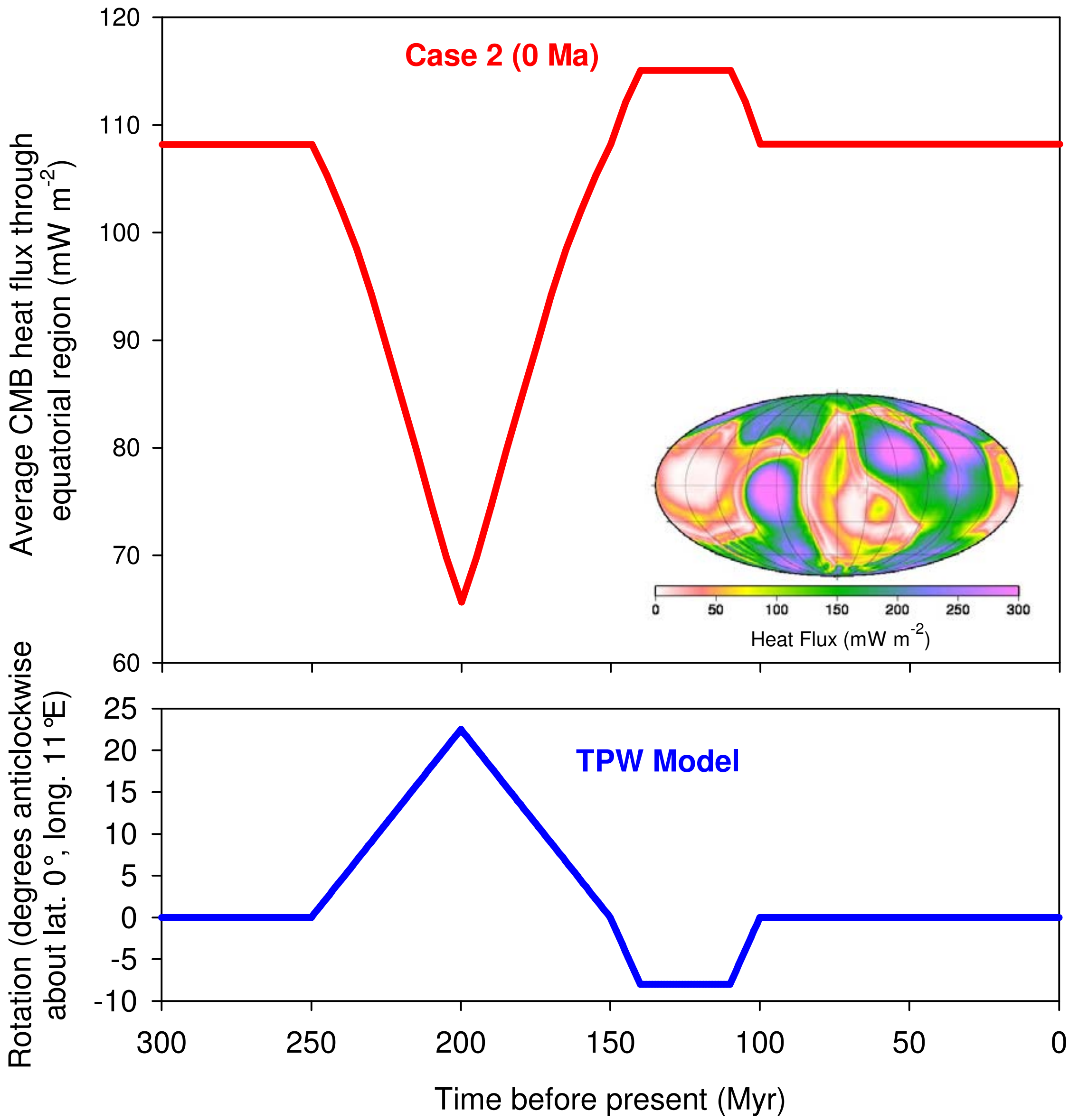

Supplementary figure 2: Equivalent analysis to that shown in figure 5 of the main text but applied to the CMB heat flow pattern produced by Case 2 for 0 Ma (shown as inset).

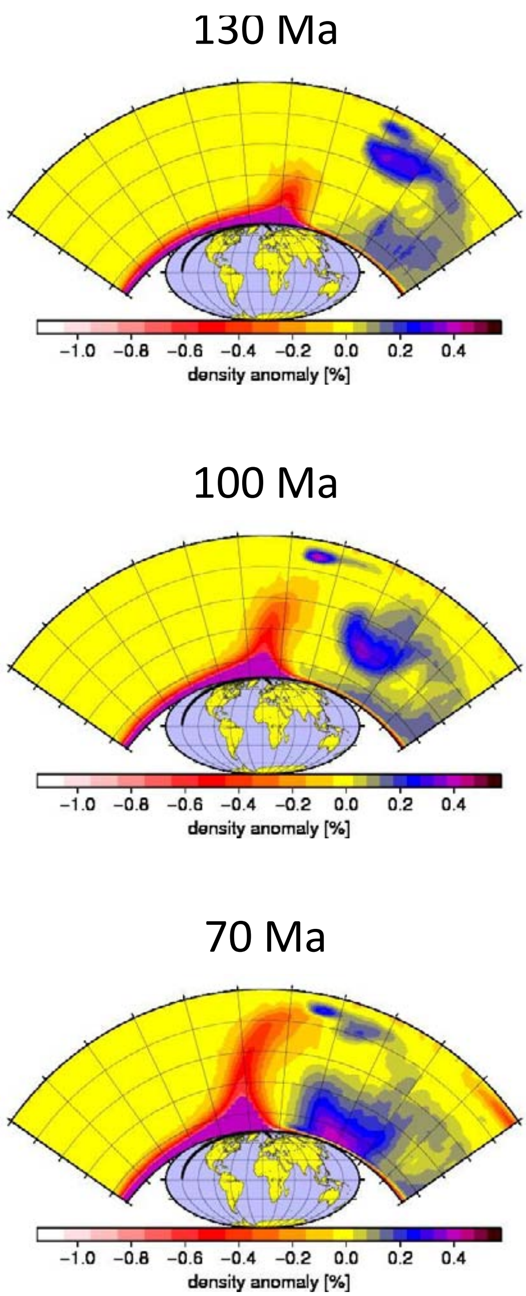

Supplementary Figure 3: Cross-sections of mantle flow model (Case 2) along the section shown at three different time points (see also figure 2c). These demonstrate the “pushbroom” effect whereby a falling slab (blue) causes a plume (red) to rise from the margin of a thermochemical pile (purple).